

Chapter 7

Plasma Torch Operational Characteristics in Quiescent and Supersonic Environments

*"Research is what I'm doing when I don't know what I'm doing."
Wernher von Braun*

This chapter presents the results of fundamental spectrographic studies of the plasma torch conducted in the quiescent environment, and the results of tests conducted in the supersonic tunnel with methane, ethylene, and nitrogen. The tests were designed to evaluate the anode geometry selected on the basis of results presented in earlier chapters, as well as provide a fundamental understanding of processes associated with various feedstocks and changes in torch power. Spectrography, total temperature sampling, high-speed photography, shock angle measurements and surface oil flow techniques were used to evaluate the design and collect fundamental data associated with plasma torches in supersonic flow. The spectral measurements, and total temperature results with methane are presented in Chapter 6, and will not be repeated here.

The work conducted in the quiescent environment focused on determining the concentration profile of excited species within the plasma jet by means of a spectrometer and motorized positioning device. Spectral measurements of the plasma jet were used to assess how the spectral intensity of these radicals changed with variations in the methane flowrate and torch power. One-dimensional analyses were conducted along the jet centerline to evaluate the intensity and propagation distance of the excited species within the jet. Additionally, spectrographic data was taken in a 2D-array pattern around the plasma jet to evaluate how the spectral intensities changed along the jet axis as well as away from the jet axis. As a whole, the spectral measurements showed that increases in the mass flowrate and decreases in the torch power both caused a decrease in the intensity of the jet. Furthermore, neither was shown to significantly affect the propagation distance of the excited species. To complement the spectrographic studies, a high-speed digital camera with spectral filters was used to capture unsteady effects within the plasma jet. Results from these tests demonstrated that the plasma jet more nearly resembles an arrowhead shape than a perfect cone as previously thought.

Supersonic experiments were aimed at determining the performance of the design in a supersonic crossflow for various flowrates, torch powers, and feedstocks. Evaluations were made based on spectrographic data, total temperature probing, high-speed photography, shadowgraphs, surface oil-flow visualization, and video observation. The spectrographic trends for methane are presented in Chapter 6, and subsequent tests with ethylene and nitrogen demonstrated similar trends. Shadowgraphs and surface oil-flow visualization demonstrated that the increase in the bow shock angle produced by the plasma jet was more a function of the input power rather than the mass flowrate through the torch. This was attributed to a volume effect associated with an increase in stagnation temperature and reduction of the feedstock molecular weight through dissociation. In addition, high-speed photographic observation captured interesting phenomena such as electrode emission and flame plumes emanating from the torch exit.

Under special conditions, combustion plumes in the supersonic tunnel were noticeable for both methane and ethylene feedstocks, while an afterglow was observed for nitrogen. Spectrographic measurements of each plume were taken to identify the radiating species within the plume, and in the case of nitrogen, the nature of the plume formation. Methane combustion occurred for powers above about 2300 W, attributed to the heating of the methane feedstock allowing sustained combustion in the cold tunnel environment. Operation with ethylene also produced a flame plume, but was possible at powers as low as 1500 W due to the wider flammability limits of ethylene. Nitrogen plumes were attributed to an afterglow effect and the production of NO_2 .

7.1: Experimental Setup

The equipment and experimental procedures used to collect the data presented within this chapter are discussed in Chapter 3. Any deviations from the general experimental procedures will be discussed as the data are presented. For particular sets of data, such as high-speed photos, the conditions and equipment settings are included along with those figures.

7.2: Results and Discussion

The results for the quiescent and supersonic experiments have been divided into two subsections, quiescent experimental results followed by the supersonic experimental results. The quiescent experimental results deal primarily with spectrographic analyses of the plasma jet based on changes in torch power and feedstock flowrate. Filtered high-speed photographs of the plasma jet are also presented to support the spectral work. Supersonic experimental results are divided into three subsections based on the feedstock gas tested: methane, ethylene, and nitrogen. The methane results here supplement those presented in Chapter 6 for the 90°, 2.54-mm throat length anode. The ethylene and nitrogen experiments were conducted with the same anode design, with the main focus on spectrographic and total temperature measurements.

7.2.1: Quiescent Experimental Results

7.2.1.1: Spectral Measurements of the Plasma Jet Centerline

Spectral measurements along the axis of the plasma jet were used to construct centerline profiles, from which the effects of changes in torch power and feedstock flowrate on the jet intensity could be ascertained. Table 7.1 lists the six most intensely radiating radicals identified within the jet (from Chapter 5), and the spectral lines used to produce the centerline plots. The spectral intensity around the jet due to combustion was assumed negligible compared to the high spectral intensity of the plasma jet. For these tests, a 1 mm scope was used and was moved in 1-mm increments along the jet axis during operation. Figure 7.1 shows the results from one of these tests, where the plasma jet exit is located on the left edge of each colored bar, with bright areas indicating regions of high concentration. Each colorbar represents one of the six radicals, and has been normalized so that the brightest part of the bar corresponds to the point of highest spectral intensity.

Table 7.1: Radicals and Spectral Lines

Specie	Measured Spectral Line
C ₂	516.5 nm
H ₂	600.3 nm
C	249.7 nm
H	656.3 nm
CH	431.4 nm
CN	388.3 nm

There are three major trends that can be identified from Figure 7.1. First, the concentrations of all the radicals do not have the same profile; some radicals reach the ground state faster or slower than others. Second, the highest spectral intensity is not necessarily located at the plasma torch exit as one might expect. As an example, the excited hydrogen intensity reaches a maximum 1 mm from the torch exit. This point, where the hydrogen intensity is at a maximum, will be identified as the boundary between the dissociation and recombination regions. Expectedly, excited C_2 and H_2 extend farther along the plasma jet axis than excited C or H atoms, due in part to recombination but also to the stable nature of the molecules. At a distance of 8 mm from the torch exit the spectral intensity was nearly zero for all wavelengths, indicating the point at which the concentration of excited species was low enough to assume that this region was just beyond the tip of the plasma jet.



Figure 7.1: Radical Concentrations Along the Centerline of the Plasma Jet

The centerline experiments were repeated for various flowrates and powers to determine how these variables affected the spectral intensity of the jet. For these experiments the H_β line was chosen as the line to be measured since hydrogen atoms are known to enhance combustion. Figure 7.2 shows the results of these experiments for input torch power variations. As expected, increases in torch power increase the spectral intensity of the H_β line, indicating a higher concentration of excited hydrogen atoms for these conditions. However, it is also interesting to note that the input power has little

effect on the propagation distance, or more accurately, the lifetime of excitation of excited hydrogen. Under these conditions, the increased arc energy creates a higher plasma temperature and concentration of excited species, but increased radiation to the surroundings prevents the propagation distance from being lengthened significantly.

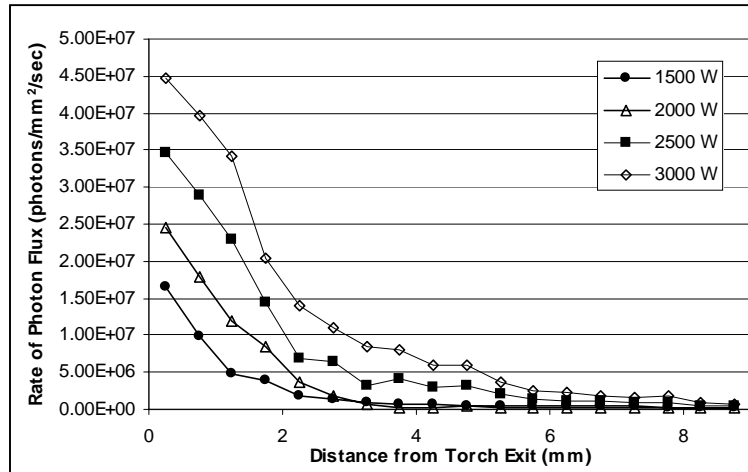


Figure 7.2: H_{β} Intensity Variations Along the Jet Centerline

Comparisons of the spectral maxima in Figure 7.2 shows a linear increase with respect to torch power, that is, every increase of 500 W produces nearly the same rise in spectral intensity. As discussed earlier, the length of the plasma jet is not significantly increased for higher powers due to increased radiation. The rate of radiation is proportional to the slope of the curve at each point, and becomes clear when comparing the slopes for the 3000-W and 1500-W case. However, the fact that the maximum observed intensity increases linearly with power is not meant to imply that the average radical concentration within the jet increases linearly as well. For this, the average rate of photon flux over the length of the jet must be measured and has been presented in Figure 7.3 for each power. From the figure, the average rate of photon flux shows a slight exponential dependence on the torch power, indicating an exponential increase in excited hydrogen concentration within the jet. Admittedly, the results from the emission spectrography do not account for hydrogen atoms in the ground state, which are still quite reactive and useful for combustion enhancement. It will be assumed that the concentration of hydrogen atoms in the ground state is proportional to the concentration of excited hydrogen atoms, so that the emission qualitatively represents the ignition

potential of the system. Continuing, if the ignition potential is directly proportional to the concentration of excited hydrogen atoms within the plasma jet, Figure 7.3 predicts that a torch operating at 3000 W would be almost three times as effective as two torches operating at 1500 W. Naturally, this type of assumption excludes any type of spatial dependence on the ignition potential.

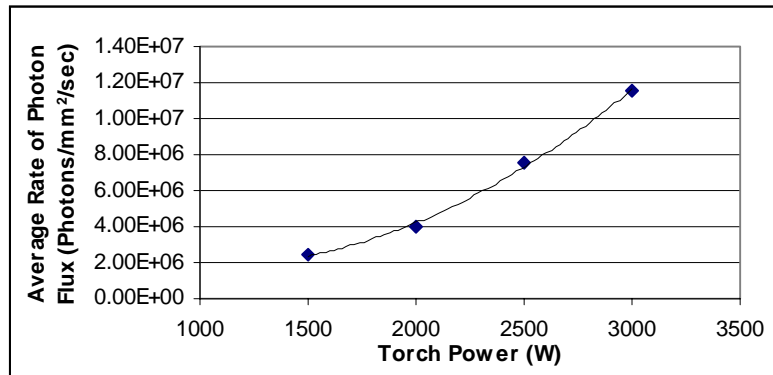


Figure 7.3: Average Rate of Photon Flux Along Jet Centerline

Increases in the feedstock flowrate produced the opposite effect of increases in torch power, that is, higher mass flowrates produced lower H_{β} line intensities along the entire axis of the jet. This reduction is due to an increase in the thermal mass of the feedstock gas, and is discussed in more detail in Chapter 6. It was theorized that the higher mass flowrates would cause a lower spectral intensity at the torch exit, but because of higher jet velocities, may cause the radicals to propagate further along the jet axis. As shown in Figure 7.4, this was clearly not the case. Radiation effects and radical recombination reactions are so quick that when compared to the low, subsonic velocities of the jet, minor increases in the jet velocity through increases in mass flowrate have a negative effect on the radical propagation distance. This suggests that plasma torches operating at a lower feedstock flowrate would have greater ignition potential due to the higher concentration of excited hydrogen atoms within the jet.

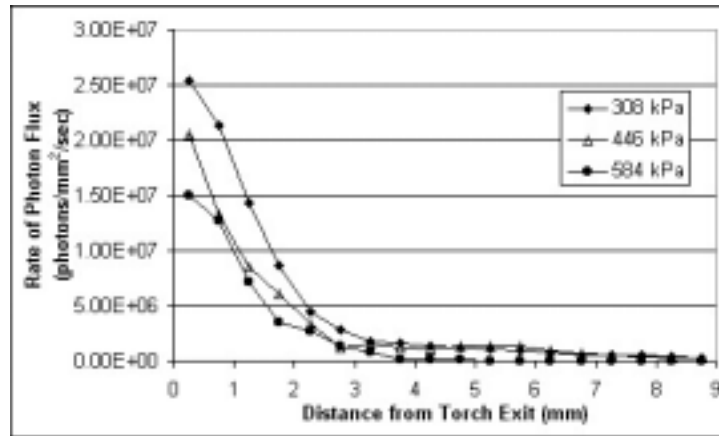


Figure 7.4: H_{β} Intensity Variations for Changing Flowrate (20 A)

7.2.1.2: Two-Dimensional Ion Concentration Profiles

The next step in the spectrographic study of the plasma jet was to create ion concentration profiles, expanding the one-dimensional knowledge of the plasma jet centerline to include the entire plasma jet. Spectral measurements of the plasma jet were made in an 8-mm by 5-mm array, for a total of 40 data points. The intensity of the spectral lines listed in Table 7.1 were then plotted to produce the ion concentration profiles show in Figure 7.5. As in Figure 7.1, the plasma torch exit is in the center-left of each profile and flow is from left to right. Brighter areas represent higher concentrations than darker areas and are measured from the maximum spectral intensity for each respective radical plotted. Although the data presented here are two-dimensional representations of a three-dimensional phenomenon, they are presented as a means by which to compare the distribution of radicals within the jet, not to represent the actual three-dimensional spatial concentration of a particular radical.

The trends observed from Figure 7.1 are evident in Figure 7.5 as well. Excited C_2 and H_2 propagate the furthest from the torch exit, while monatomic carbon and CH propagate the shortest distance. The lateral spread of these radicals matches the same trend as with the propagation distance along the jet centerline. Immediately, this points to a temperature effect in which the temperature is known to decrease both radially and along the jet axis. This is quite plausible considering the concentration of an excited specie is directly proportional to the temperature of the region, according to the Saha equation presented in Chapter 6. From this, it can be concluded that if one wants to increase the penetration distance of a particular radical, then higher plasma temperatures

must be obtained. However, this effect will naturally be balanced by an increase in radiation as demonstrated in Figure 7.2. Therefore, to enhance the ignition potential of a plasma torch as an igniter, effort should be concentrated on increasing the concentration of combustion enhancing radicals rather than the penetration distance of such radicals. The penetration distance can be improved by means of an outside device such as an aeroramp, as demonstrated in Chapter 9.

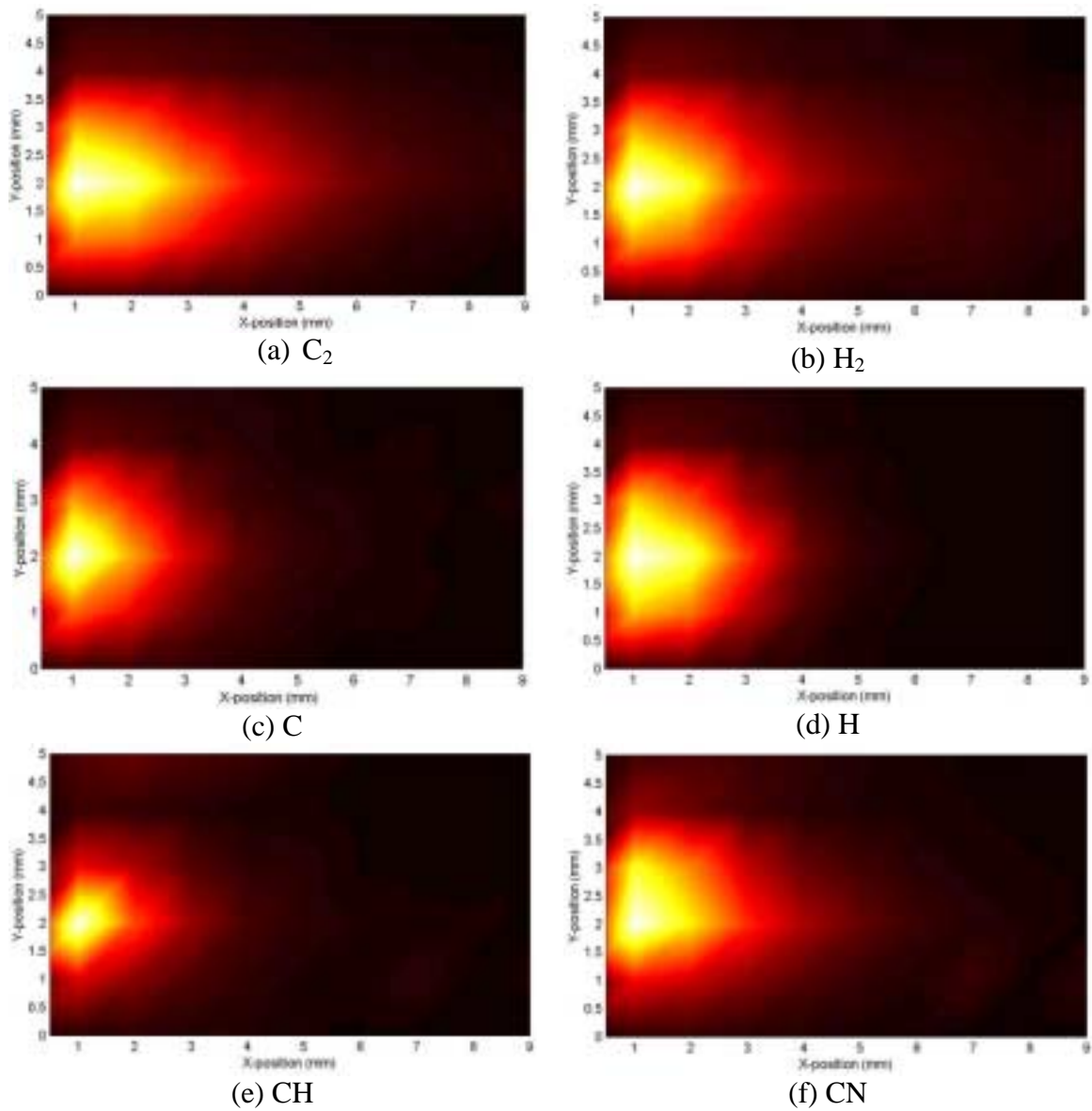


Figure 7.5: Ion Concentration Profiles

7.2.1.3: High Speed Visualization

A high-speed digital camera, with various spectral filters, was used to support the findings of the spectrographic work and also to observe unsteady effects within the plasma jet that the spectrometer could not capture. The test conditions and camera settings are included with each figure. Also, all high-speed pictures are presented so that the torch exit is in the center-left of each frame and flow is from left to right.

Figure 7.6 shows samples of high-speed digital photographs taken through the spectral filters. Here the photographs are separated into two columns depending upon whether the observed radical is a hydrocarbon fragment or contains an atom associated with air (N or O). It is clear when comparing the filtered photographs for C_2 , H_2 , and CH that the relative distances the radicals extend beyond the torch exit are similar to those presented in Figure 7.1; that is, C_2 and H_2 propagate roughly the same distance, with CH being much shorter-lived. Close observation also reveals that buoyancy effects are present, shown by the slight lifting of the plasma jet near the tip. The hydrocarbon-air interaction photographs are presented for both OH and CN, species produced when the hot hydrocarbon plasma interacts with the surrounding air. It is clear that they are much dimmer than the hydrocarbon fragments, supporting the earlier assumption that combustion surrounding the plasma jet does not contribute significantly to the spectral intensity measured by the spectrometer. In addition, they both exhibit a hoop structure, whereas the hydrocarbon fragments show a “solid” profile.

The hoop structure exhibited with the excited OH and CN molecules is thought to be a function of the shape of the plasma jet and was studied further. Although the plasma jet appears to have a cone-like structure, it was theorized that the plasma jet was actually more of an arrowhead shape, relatively flat along one axis and broad on the other. Figure 7.7 shows a graphical representation of this theory. It is believed that because of the rapid rotation of the arc, this arrowhead appears as a cone. Excited hydrocarbon fragments are present within the arrowhead region, with undissociated methane forming a boundary between the plasma and surrounding air. The arrowhead theory suggests that reactions leading to the formation of OH and CN would occur only along the edges of the arrowhead structure, since the flat sides are surrounded by pure, undissociated methane and would prevent interaction with the surrounding air.

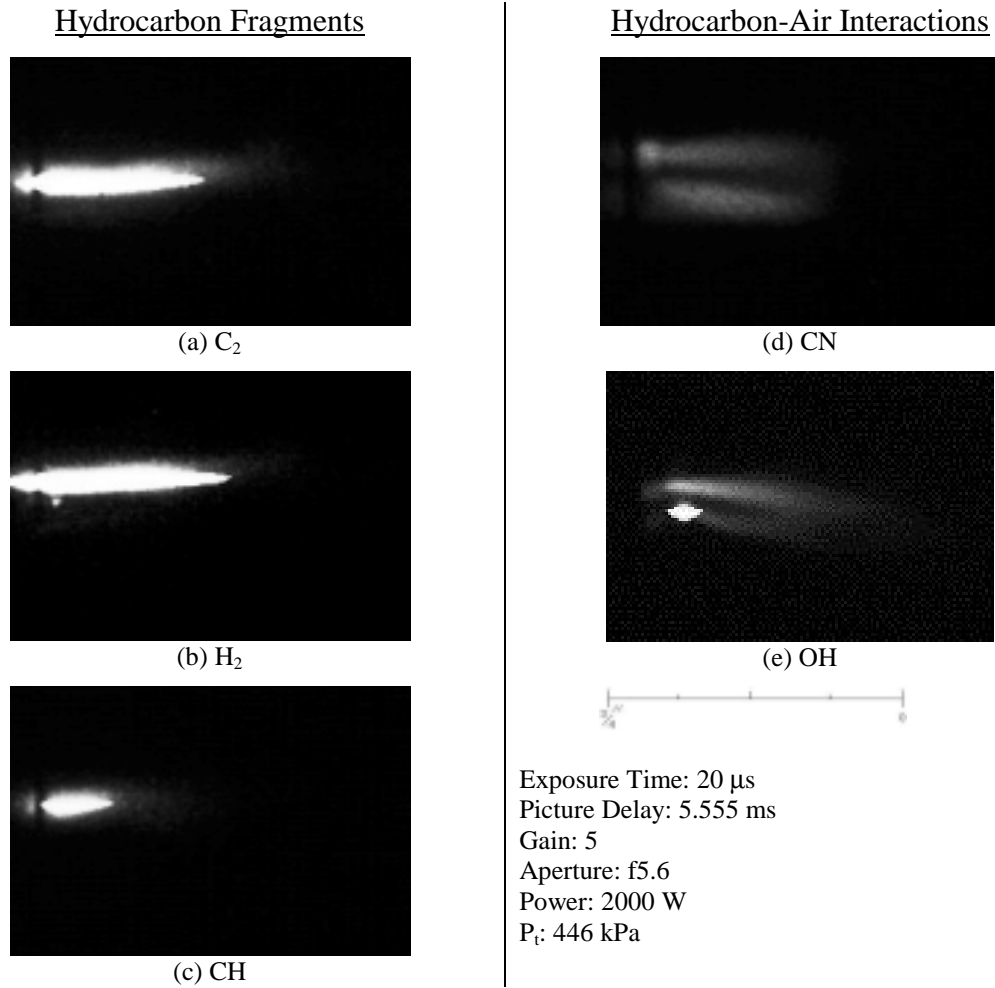


Figure 7.6: High-Speed Filtered Photographs

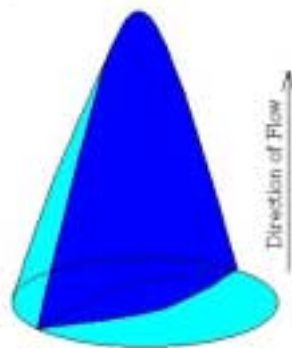


Figure 7.7: A Graphical Representation of the Arrowhead Theory

The arrowhead theory was investigated by means of further observation of the plasma jet through the OH and CN filters. By taking sequential pictures of the plasma jet through these filters, the hoop structures were observed to rotate about the jet centerline,

as shown in Figures 7.8 and 7.9, for both excited OH and CN molecules. The bright spot in each frame of Figure 7.8 is the arc attachment point and was observed to rotate about the plasma torch exit, which is indicated by the arrow. A well-defined hoop structure can be seen in Figure 7.8a, starting from the plasma jet exit and ending at the arc attachment point. The brightest portion of the hoop is near the base of the jet, where the temperature and radical concentrations are highest. The frame in Figure 7.8b was taken 5.555 ms after the frame in Figure 7.8a to ensure that the two pictures were taken at the same point in the voltage cycle. In this view, the arc attachment point is directly behind the plasma torch exit and the hoop structure seems to disappear as the camera looks across the plane of the hoop. In addition, by observing the rate of rotation of the arc attachment point around the torch exit, the arc rotation rate was estimated to be between 5 and 10 Hz. This rotation frequency is a function of the swirl number of the flow, in this case 1.0. (The swirl number for a rotating flow is defined as the ratio of tangential velocity to axial velocity.)

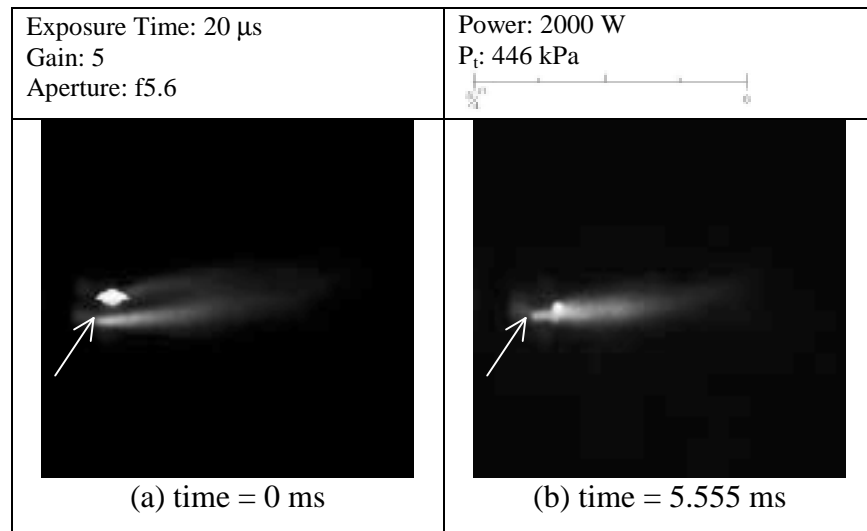


Figure 7.8: OH Visualization of Plasma Jet

The same trends observed in Figure 7.8 for OH are observed in Figure 7.9 for excited CN. For this spectral wavelength the arc attachment point is not as obvious, so the exposure time of each photograph was increased to 200 μ s, resulting in the grainy appearance of the photo. Figure 7.9a shows the characteristic hoop structure for excited CN. As with Figure 7.8b, Figure 7.9b shows the hoop structure being observed along the

edge of the hoop. As with the OH hoop, the brightest portion occurs near the base of the jet. This hoop structure, observed at two separate wavelengths, identifying two separate molecules, confirms that the hoop structure is produced through air-plasma interactions. Furthermore, these reactions are confined to an area where the plasma jet is in direct contact with the air.

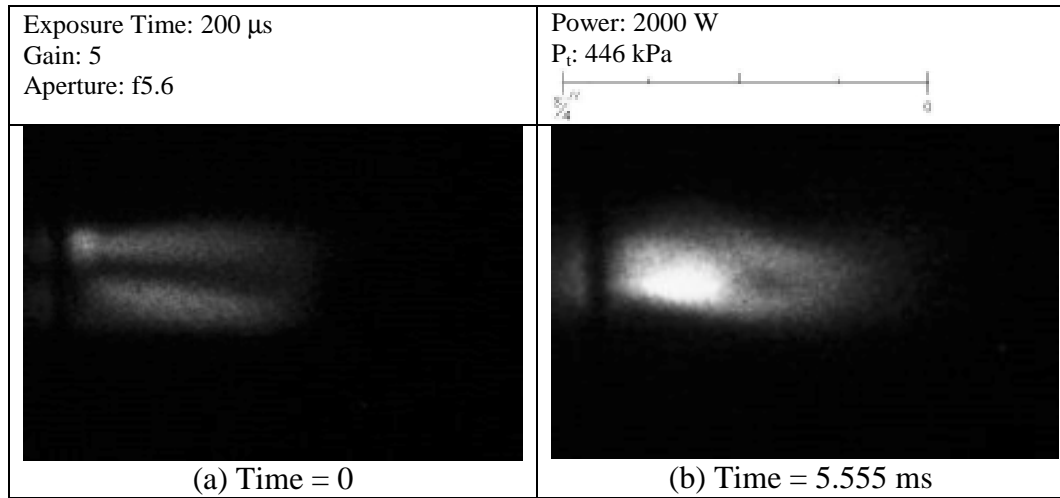


Figure 7.9: High-speed Photographs of CN within the Plasma Jet

To further support the arrowhead theory, high-speed photographs were taken down the axis of the plasma jet using mirrors. The goal was to determine if the plasma jet appeared flat or circular along this axis of observation. For this study, a hydrogen filter was chosen because excited hydrogen atoms have a very small recombination time, and hence would be more representative of the plasma jet shape near the torch exit. Tracking C₂ molecules in this way may capture effects near the middle or tip of the jet where the C₂ molecules would spread due to diffusion and might produce a more circular profile. As shown in Figure 7.10, the photograph taken through the hydrogen filter clearly exhibits a flattened structure, supporting the idea behind the arrowhead theory.

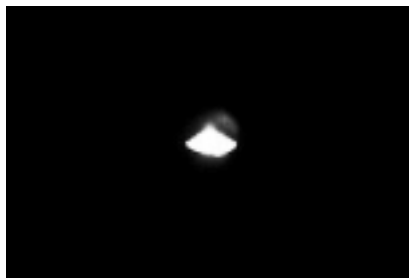


Figure 7.10: H Filtered Photograph Down Axis of Jet
(2100 W, Exp Time: 20 μ s, Gain 3, f11)

During the sequence of tests used to produce the photographs presented above, an interesting pulsation/eddy effect was observed through one of the OH filters. The photographs of this phenomenon are shown in Figure 7.11, and were taken through an OH filter that allowed wavelengths of light near 306 nm and the VIS-Red region to pass through. Since the filter allows a wide range of wavelengths to pass through, these pictures do not represent any particular radical. In spite of this, these pictures show a number of downstream eddies as they propagate along the jet axis. One of these eddies is marked by an arrow in frame 3 and again in frame 4, demonstrating the downstream propagation of such a formation. As observed with earlier work (Gallimore, 1998), these eddies are a result of the plasma jet pulsation due to the voltage fluctuations of the power supplies, and are subject of much importance since this pulsation can be used for enhancing mixing in a crossflow.

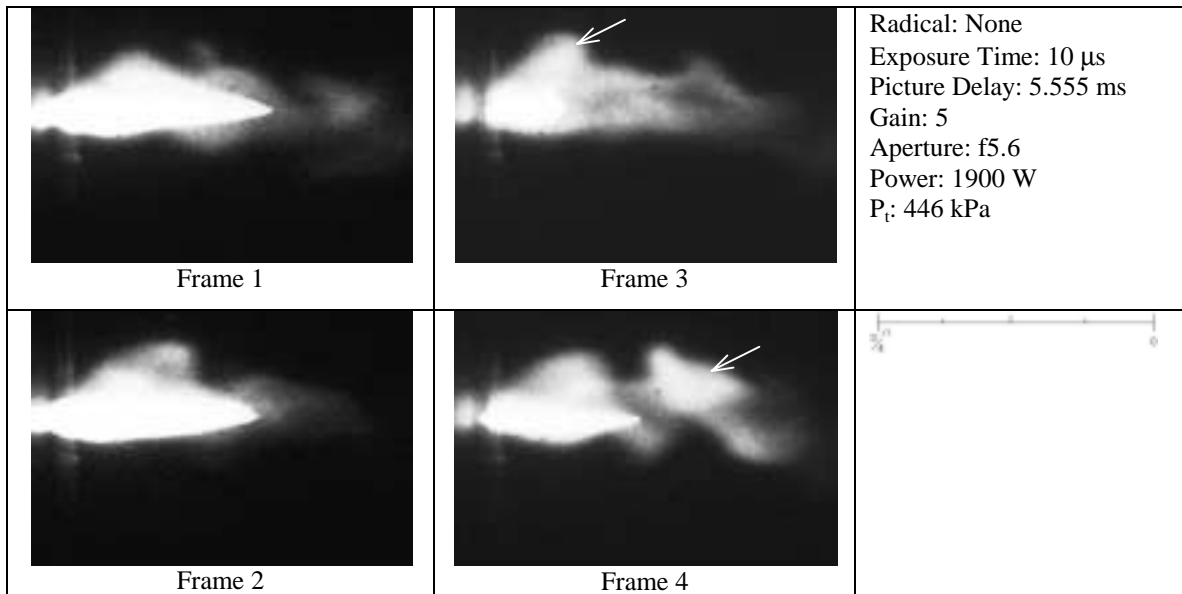


Figure 7.11: High-speed Photographs of the Plasma Jet

7.2.2: Supersonic Experimental Results

The experiments conducted in the supersonic tunnel were performed with the 90°, 2.54-mm throat length molybdenum anode, based upon the results presented in Chapters 4, 5, and 6. The total temperature and spectrographic measurements were all conducted in an unheated Mach 2.4 crossflow ($T_t = 300$ K, $P_t = 379$ kPa), with methane, ethylene, and nitrogen as the feedstocks. The discussion of these results is divided into subsections

pertaining to each of the feedstock gases. Total temperature and spectrographic measurements for methane are presented in Chapter 6, while the supporting high-speed photography, shadowgraphs, surface oil-flow visualization, and video are presented here.

7.2.2.1: Methane in Supersonic Flow

High-speed photography provided some of the most useful insight into areas where other types of measurements were unsuitable. Figure 7.12 shows two examples of this, capturing the process of electrode particle emission into a Mach 3.0 crossflow. In Figure 7.12a, the electrode particle is ejected slightly in the upstream direction and then is swept away by the crossflow to the right. The most important aspect of these two photographs is the penetration height of the tungsten particle. The particles quickly penetrate to a height of 3 to 4 cm, giving up their heat to the surrounding crossflow. In both figures, the intensity of the particle can be seen to dim as it travels downstream and cools. It was thought that a plasma torch with a consumable cathode could be used to purposefully inject these particles well out into a supersonic crossflow, which would then be able to ignite fuel (Schetz, 1999). The advantage a design of this nature would have over traditional electrode designs is that energy wasted in vaporizing the cathode material might then be available as molten particles that could be used as micro-flameholders.

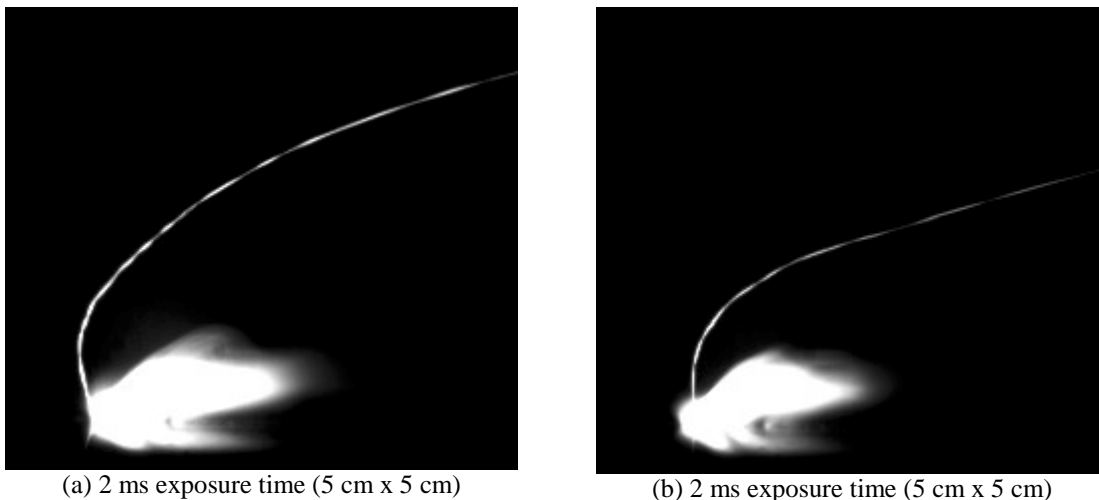


Figure 7.12: Electrode Emission in Mach 3.0 Crossflow (VTPT-2)

Video footage of the test cell demonstrated that the electrode particles remain quite hot for an extended distance, despite the cold conditions of the tunnel. The

photographs shown in Figure 7.13 are single frames taken from video footage of the plasma torch operating on methane in a Mach 2.4 crossflow. The graininess near the torch exit is due to imperfections in the window glass. Flow direction is from the bottom left to upper right and the plasma jet is the bright region in the lower left. The total temperature probe is silhouetted in the upper right side of the frame, where the distance between the probe tip and plasma torch exit is 7.87 cm. Figure 7.13a shows a large amount of electrode emission, mostly confined to the tunnel floor. These particles travel along the floor until they impact the plate used to hold the probe in place. In Figure 7.13b there is less electrode emission, but the particles here are observed to penetrate into the crossflow, similar to those shown in Figure 7.12. In addition, a short, but intense methane flame plume can be observed emanating from the torch exit.

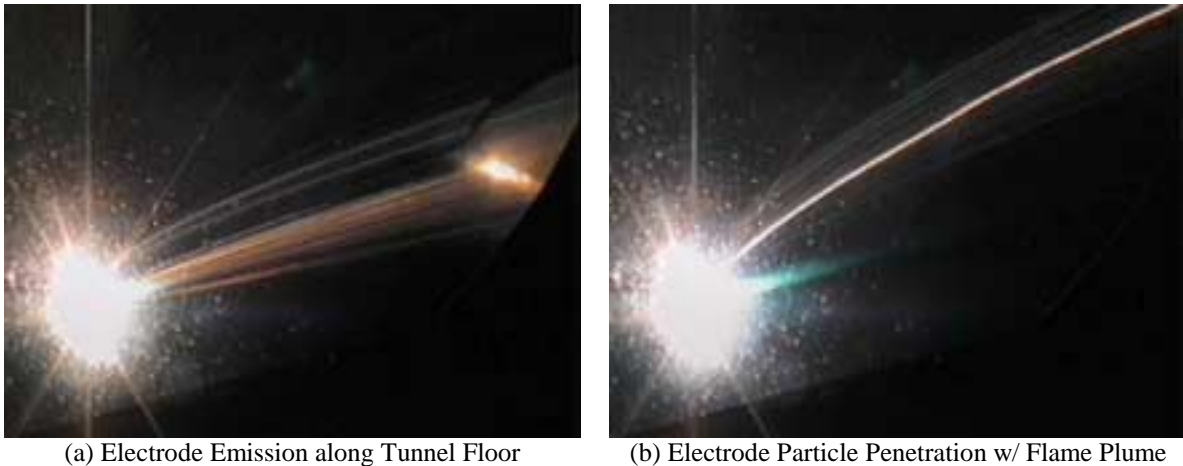
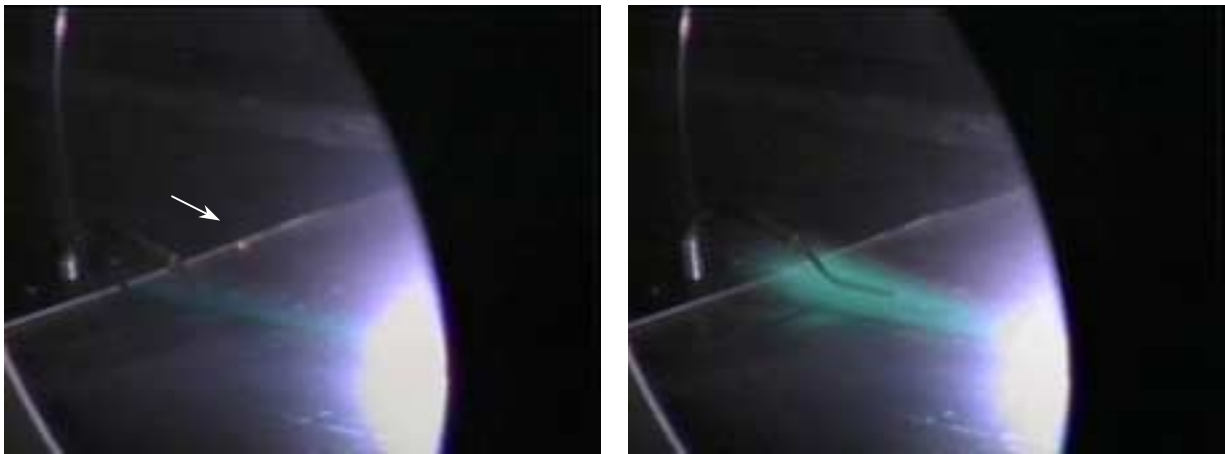


Figure 7.13: Plasma Torch Electrode Emission in a Mach 2.4 Crossflow

The flame plume produced by the torch was an exciting discovery, especially since the tunnel was unheated. In general, plasma torches dissociate only a small fraction of the feedstock gas passing through the constrictor region, perhaps as much as 10%, while the rest of the feedstock is heated through convection and radiation. A small portion of this remaining 90% is what was observed to burn in this unheated environment. The power at which the flame plume was observed to appear was around 2200 W, with higher powers producing larger, brighter flame plumes. Two video stills showing bright methane flame plumes are presented in Figure 7.14, where flow is from bottom-right to top-left. The stills are both from the same test run, but the flame plume in

Figure 7.14b appears brighter than the one in 7.14a because occasionally the flame plume would flare. In Figure 7.14a the flame plume extends beyond the probe tip, traveling about 10 cm downstream of the torch exit. An arrow highlights an area where an electrode particle has been ejected from the torch and impacted the probe plate. The flame plume in Figure 7.13b is quite bright and the temperature probe is well defined. The flame length has not changed, but the intensity and amount of burned methane have increased.



(a) Power: 3500 W

(b) Power: 3500 W

Figure 7.14: Methane Combustion Plumes in a Mach 2.4 Crossflow

A spectrogram taken of the methane combustion plume is shown in Figure 7.15 and was taken approximately 4 cm downstream of the torch exit. The plasma jet extends no further than 1 cm downstream of the torch exit so the peaks shown in this figure can be solely attributed to combustion products and intermediaries. The scale is such that the strong H_{α} line is clipped, but lower peaks are more easily recognized. When compared to the methane plasma Spectrogram of Figure 5.1, the presence of all the major species are here as well: C_2 , C, H_2 , H, CH, and CN. In addition to these species, other species associated with hydrocarbon combustion, OH, HCO, CO_2 , H_2O and CH_2O , were detected as well. The ranges that these molecules strongly radiate are labeled in Figure 7.15. One peculiarity is the relative weakness of the OH system near 306 nm, which is usually one of the strongest and most identifiable features of any flame spectra. However, the thermal radiation of OH is very weak in low-temperature and low-pressure flames, of which both conditions are present within the tunnel ($T \approx 130$ K, $p \approx 25$ KPa). Charton and

Gaydon (1958) attributed the temperature effect to some chemi-excitation of OH through the reaction



The excitation varies as the cube of the concentration of the free radicals associated with the reaction, and dies out rather quickly along the length of the flame as the excess radicals recombine. For low-pressure flames, Kondratiev and Ziskin (1937) discovered there is no well-defined reaction zone, and the (0,0) band of OH is emitted weakly from the entire body of the flame as observed here.

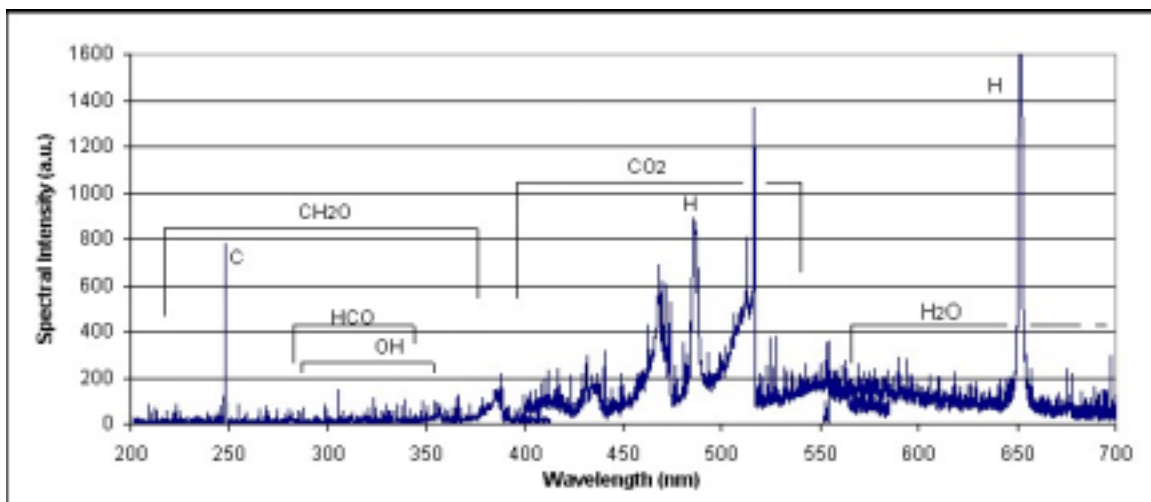


Figure 7.15: Spectrogram of Methane Flame Plume

Shadowgraphs provided a measure of the amount of flow blockage the plasma jet was creating under various operating conditions. Increases in the momentum flux ratio and the torch power were both observed to increase the angle of the bow shock upstream of the plasma jet. Figure 7.16 shows five shadowgraphs taken for a momentum flux ratio of 0.80 and a power range of 0 to 3750 W, where flow is from right to left. The bow shock angle is measured from the point at which the bow shock penetrates the boundary layer, A, to the tip of the bow shock at the edge of the frame, B. A horizontal line identifies the edge of the boundary layer. Increases in torch power were observed to have a slight increase on the bow shock angle, from 28° for no power to 32° for 3750 W, a little less than one degree per 1000 W. Admittedly, the difference is slight, but important. The increase in the shock angle is related directly to the amount of volume addition, not mass flowrate, which remains roughly constant throughout the power range.

Furthermore, the increased volume addition is a result of the arc energy being transferred to the feedstock gas, which results in an increase in the total temperature of the gas and a decrease in the molecular weight. Chrans and Collins (1970) studied the effect of stagnation temperature and molecular weight effects on shock shapes in supersonic flow and derived a term for the characteristic radius of the bow shock according to

$$R_o = \left[\frac{\dot{m}_j V_\infty}{\pi P_\infty} \left(\frac{1}{2} + \frac{1}{\gamma_\infty (\gamma_\infty - 1) M_\infty^2} + \frac{\gamma_j}{\gamma_j - 1} \left[\frac{2 + (\gamma_\infty - 1) M_\infty^2}{2 \gamma_\infty M_\infty^2} \right] \left[\frac{W_\infty T_{oj}}{W_j T_{o\infty}} \right] \right) \right]^{1/2} \quad (7.2)$$

where W , and T_o are the molecular weight and total temperature of the gas, respectively, and the subscript j refers to the jet. Here, the characteristic radius of the bow shock, R_o , is related to the actual radius of the bow shock defined by Sakurai (1953) as

$$R = \left(\frac{2R_o}{J_o^{1/2}} \right)^{1/2} \left(\frac{x}{M_\infty} \right)^{1/2} \quad (7.3)$$

where J_o is a nondimensional constant depending upon the ratio of specific heats, and x is distance in the primary stream direction. From equations 7.2 and 7.3, for a constant mass flowrate, both an increase in the total temperature of the jet and a decrease in the molecular weight of the jet will cause an increase in the bow shock radius. As stated earlier, these are both translated into volume effects. Essentially, for a given mass flowrate, the addition of volume will cause the freestream to deflect in order to make room for the added gas and pressure field generated (Broadwell, 1963). Consequently, this results in a stronger shock with a larger radius and shock angle, as observed here. The result is an increase in the total pressure losses associated with the igniter, although from a system viewpoint, the total pressure losses associated with the igniter are relatively minor compared to the losses induced by the main fuel injection.

Chrans and Collins (1970) noted that the increase in the bow shock angle and radius were related to the jet momentum, not the jet mass flowrate. Increases in the momentum flux ratio through the increase in mass flowrate were observed to have a negligible effect on the position and angle of the bow shock, as shown in Figure 7.17. Here an increase in the momentum flux ratio from 0.80 to 1.15 produces no observable increase in the bow shock angle. Referring to equation 7.2, this is mainly due to the change in the \dot{m}_j term being so small. More importantly, over the range of powers

presented here, the bow shock angle increases by about one degree per 1000 W. In addition, the forward separation zone increases slightly with increasing torch power, which is evident by comparing the bow shock position on the floor of the tunnel for Figures 7.17a and 7.17e. For the operational range of the torch, this demonstrates that the effect of heat addition is much greater than the effect of mass addition on the momentum of the jet, and the subsequent change in bow shock angle.

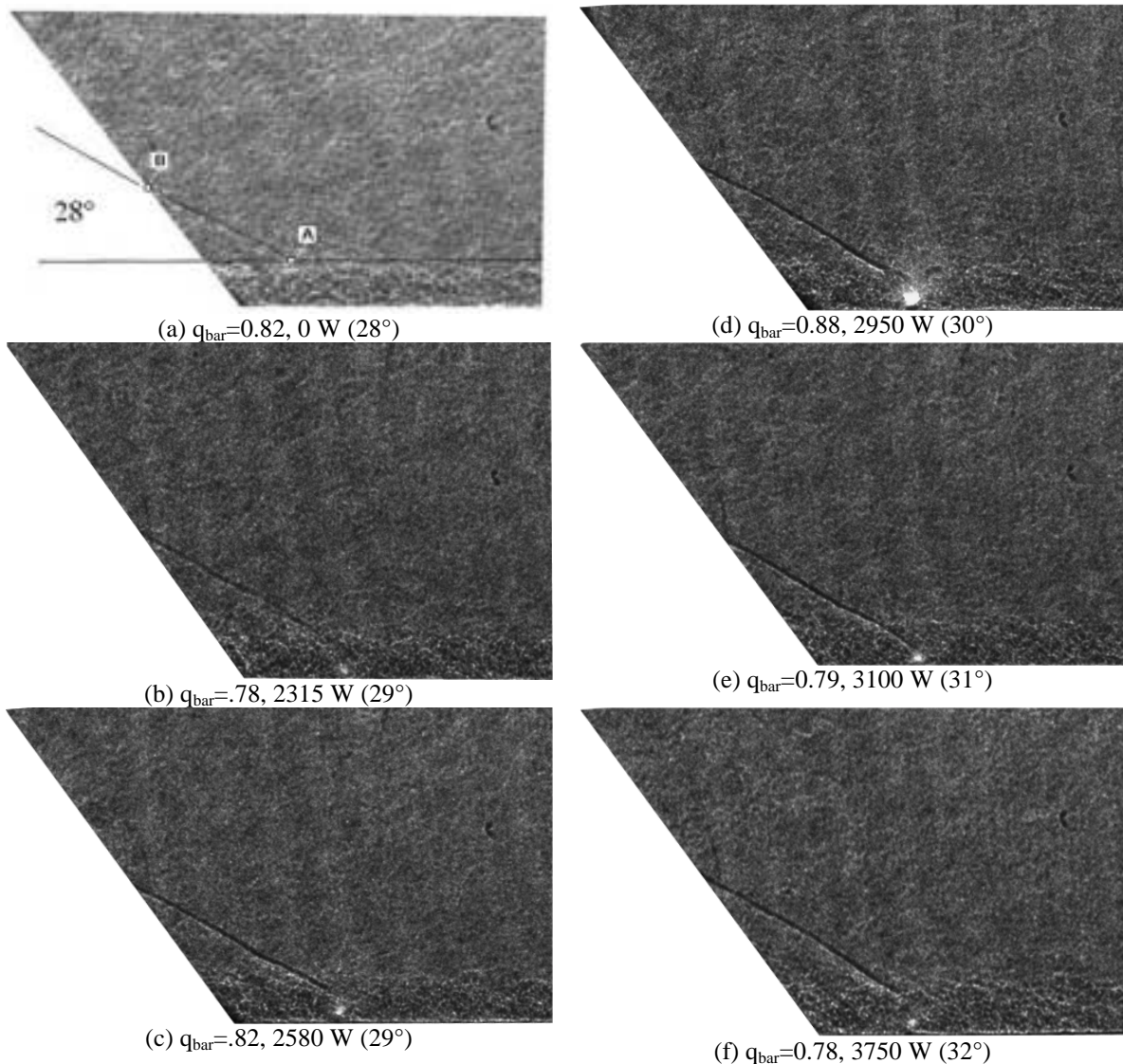


Figure 7.16: Shadowgraphs for a Momentum Flux Ratio of 0.80

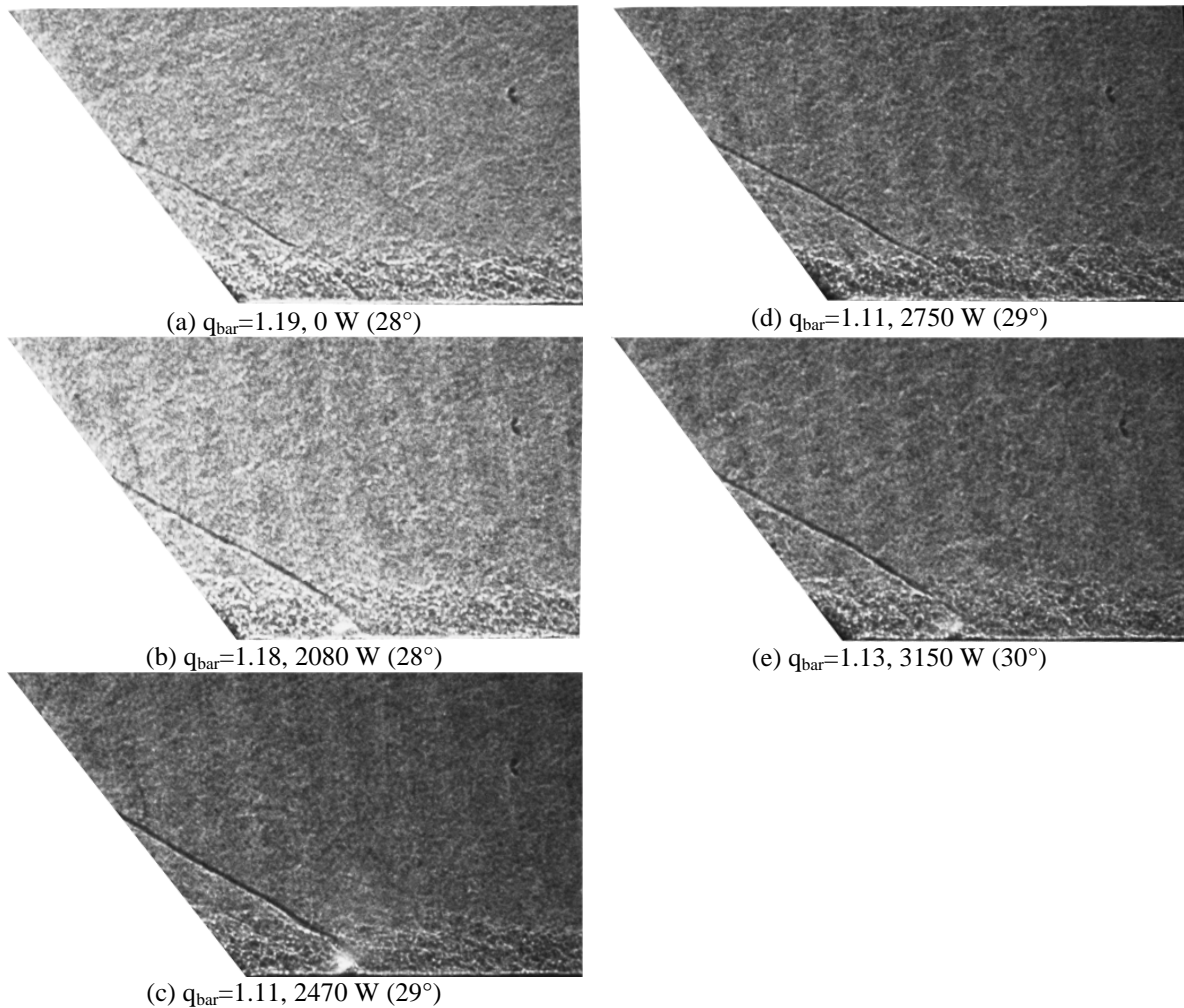


Figure 7.17: Shadowgraphs for a Momentum Flux Ratio of 1.15

Only when the momentum flux ratio was increased to 2.3 did the effect of the mass addition produce any noticeable effect. As shown in Figure 7.18, the bow shock angle increases to 29° , as compared to 28° for the lower momentum flux ratio cases. A tripling of the momentum flux ratio causes only a one-degree increase in the bow shock angle, while it appears to increase by one degree for every 1000 W of input power, as with the previous cases. This further supports the point that the total pressure losses induced by the plasma torch are more a function of the input power than the mass flowrate. Each of the momentum flux ratio cases experiences the same angle change for increases in torch power, indicating that for the flowrates tested, the effect of power addition on the bow shock angle is independent of the mass flowrate. According to Equation 7.2, this should not be the case since the total temperature rise and increase in

the molecular weight is directly proportional to the amount of energy the arc transfers to the gas. For a given power input, higher flowrates will experience less change in these values simply through the addition of extra mass in which to distribute the energy and prevent dissociation. It is predicted that power effects on the bow shock angle should be more observable at lower flowrates since the rise in temperature and dissociation percentage of the feedstock gas is greater.

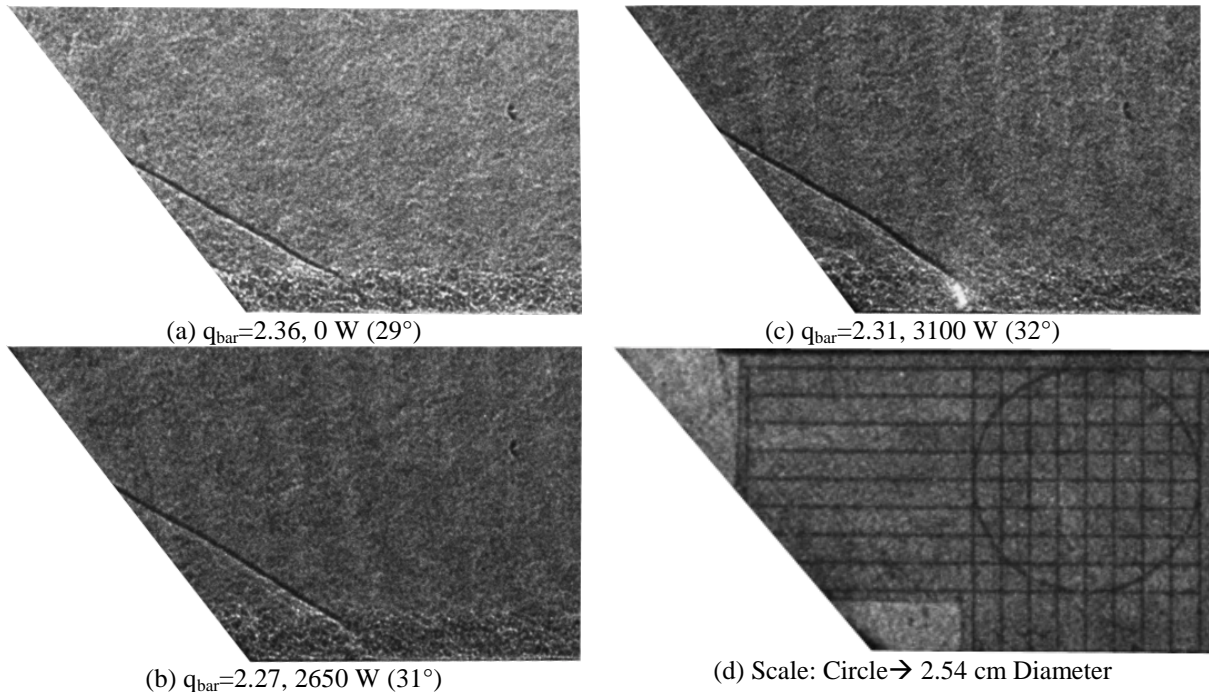


Figure 7.18: Shadowgraphs for a Momentum Flux Ratio of 2.30

Oil-flow visualization techniques provided insight into how the momentum flux ratio and input power affected the surface flow near the tunnel floor. A diagram of a typical oil-flow picture is shown in Figure 7.19, where the different regions of importance are labeled. Figure 7.20 shows actual oil-flow pictures for four separate methane runs. Comparison of Figure 7.20a and 7.20b demonstrates that increasing the momentum flux ratio strengthens and widens the bow shock upstream of the torch exit. Also, the bow shock has been pushed further upstream, increasing the size of the separation region just upstream of the torch exit. Downstream of the torch exit, increases in the momentum flux ratio broaden the area affected by jet expansion and expand the size of the separation zones. The presence of a plasma jet disrupted the flow region

downstream of the torch, so that these regions were no longer identifiable. However, for both momentum flux ratios, the width of the bow shock increases as shown in Figure 7.18c and 7.18d, indicating an increase in the volume, or blockage of the jet as discussed earlier.

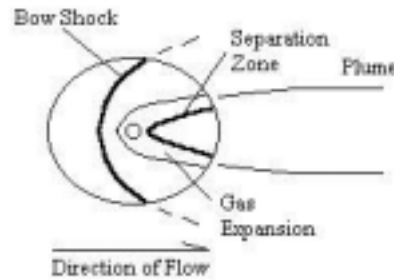


Figure 7.19: Diagram of Surface Oil-Flow Patterns

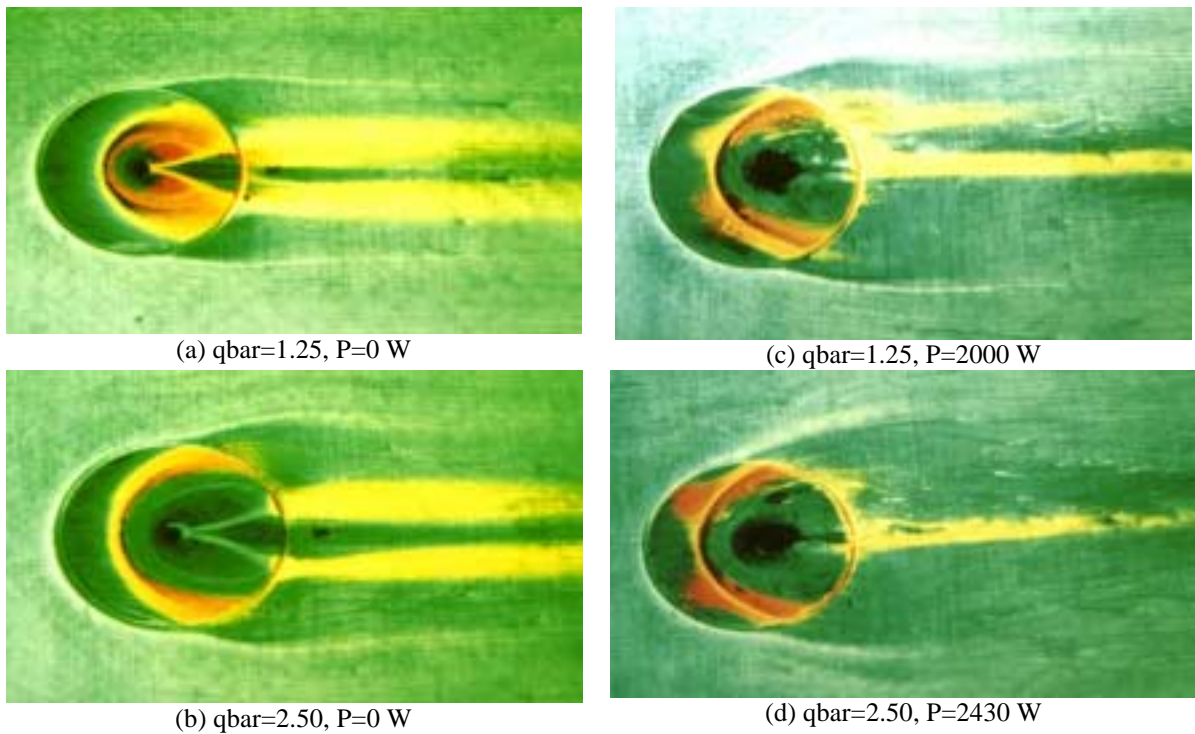


Figure 7.20: Surface Oil Flow Pictures (Methane)

7.2.2.2: Ethylene in Supersonic Flow

A number of spectrographic surveys of the ethylene plasma jet were taken across the torch exit to determine how the intensity of the H_{β} line changed with power and also how these results compared to line intensities produced with methane. Figure 7.21 is a

plot of the maxima of these profiles. (A sample exit profile is shown in Figure 6.6 as a reference.) As with the methane work, the spectral intensity of the H_{β} line increases linearly with power. In addition, it is interesting to note that the spectral maxima of the exit profiles for methane map directly onto the same trend line, that is, the slope and position of the two trend lines are nearly identical. Although full two-dimensional profiles would provide a better comparison, this suggests that methane and ethylene have the same hydrogen radical production rate for a given power. Based upon operational lifetime and stability, methane would be a better choice.

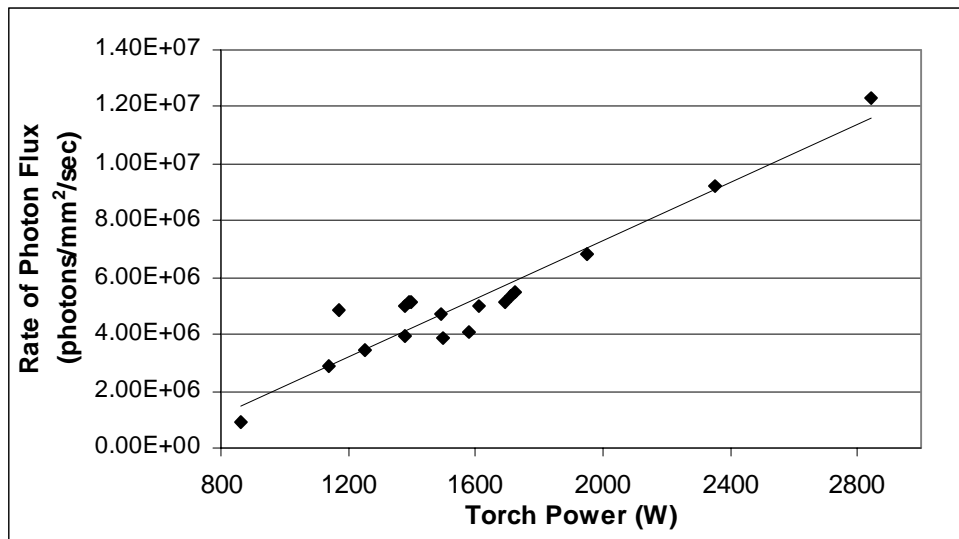


Figure 7.21: Intensity of H_{β} Line versus Power for Ethylene ($q_t=1.14$)

Total temperature measurements downstream of the torch showed trends similar to temperature measurements in the methane experiments presented in Chapter 6. As expected, the maximum total temperature ratio increases with torch power and the penetration height shows little dependence on the amount of energy imparted to the gas by the arc. However, comparison of these results to the centerline temperature measurements for methane in Figure 6.13 shows that, for a given power, the ethylene produces a higher total temperature ratio. One might expect that this difference could be attributed to heat release through combustion. However, the heat release by combustion is much smaller than the energy imparted to the feedstock by the arc, particularly since the amount of fuel combusting is small in this low static temperature and pressure environment. In addition, below 1800 W, neither methane nor ethylene feedstocks

produced flame plumes so the added contribution to the temperature rise in these cases would be zero. The difference in total temperature is directly proportional to the difference in specific heat between the two gases. It is well known that a gas with a higher specific heat will extract more thermal energy from an electric arc. At an assumed bulk temperature of 1000 K, the specific heat of ethylene is 93.80 kJ/kmol•K, compared to 71.60 kJ/kmol•K for methane. Upon injection, this energy is then distributed to the air. Although thermal equilibrium is not attained by the time the flow propagates downstream to the temperature probe, the energy imparted to the surrounding air is greater for ethylene, causing a higher total temperature.

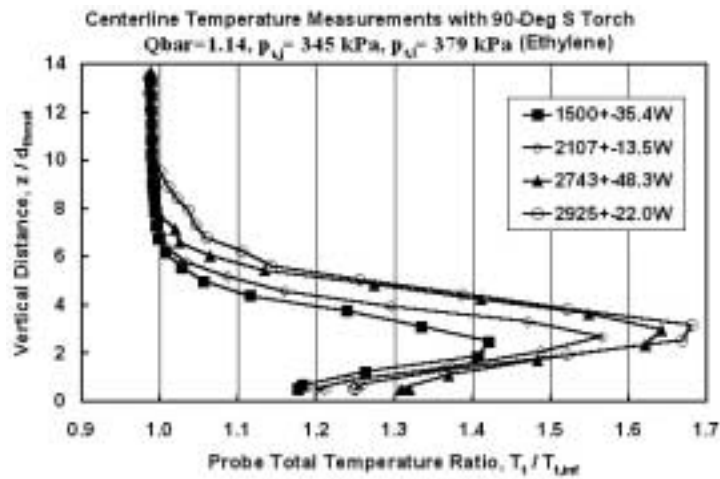


Figure 7.22: Ethylene Centerline Temperature Profiles

A 2D total temperature ratio plot for ethylene at 1500 W and a momentum flux ratio of 1.14 is shown in Figure 7.23. Comparison to Figure 6.14a, methane under the same conditions, shows that the penetration height is somewhat lower, but the total temperature ratio for ethylene is much higher, 1.42 compared to 1.26. The ethylene plume also appears narrower, caused by the higher molecular weight of ethylene, which is related to the diffusivity of the molecule. Finally, the core of the plume is shifted one diameter to the left, indicating that the swirl has affected the downstream position of the core.

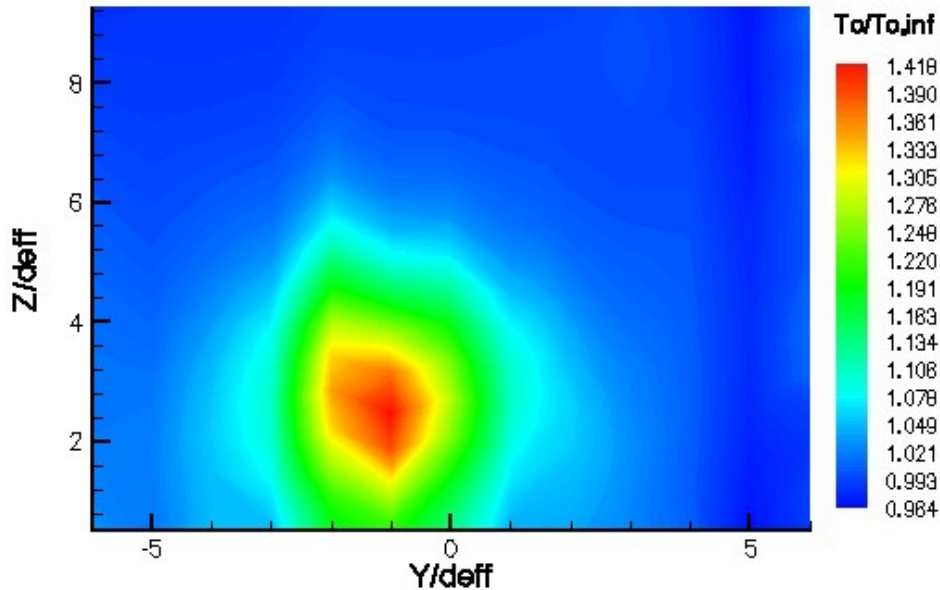


Figure 7.23: Two-Dimensional Temperature Profile for Ethylene
($q_t=1.14$, 1500 W)

For torch powers of 1500 W or above, the ethylene plasma jet ignited a small fraction of the remaining ethylene not previously dissociated by the torch. A typical ethylene flame plume is shown in Figure 7.24 where flow is from left to right. The flame plumes of ethylene were typically much brighter than those of methane. Gaydon (1974) notes that fuels with higher carbon contents produce the most luminous inner cones for flames, in agreement with the observations presented here. The limit of ignition for ethylene under these conditions was about 1500 W, 800 W lower than methane due to the wider flammability limits of ethylene.



Figure 7.24: Ethylene Flame Plume in Mach 2.4 Crossflow

7.2.2.3: Nitrogen in Supersonic Flow

Spectrographically, the plasma jets produced by the nitrogen feedstock in the supersonic tunnel were difficult to evaluate because of their low relative intensity and the

short run time of the tunnel. These conditions required a longer exposure time to be used, resulting in fewer data points. Despite these difficulties, spectrographic observation of the plasma jet showed that the spectral signature of the nitrogen plasma in the Mach 2.4 crossflow was the same as for the jet in the quiescent environment. In addition, as with the hydrocarbon feedstocks, a linear relationship between the power and spectral intensity of the jet was observed. This is demonstrated in Figure 7.25, where the spectral maxima for a strong N₂ line in the Second Positive System for nitrogen are plotted versus power.

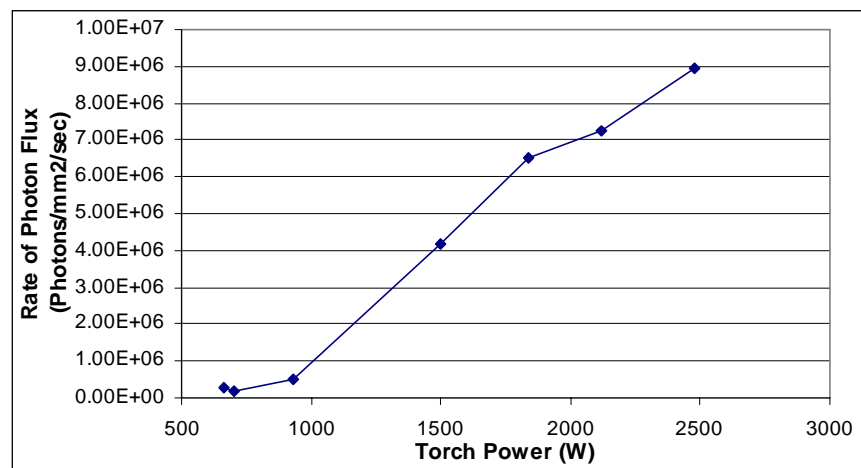


Figure 7.25: Spectral Intensity of N₂ Molecule at 380.5 nm ($q_t=1.2$)

In addition to the plasma jet, a luminous plume of emitting species originating at the torch was observed, similar to the flame plumes observed with methane and ethylene. The spectral signature of the plume, shown in Figure 7.25, is quite similar to the nitrogen plasma spectrograms presented in Chapter 5. This spectrogram was taken 1.3 cm downstream of the jet, rather than 4 cm as for the hydrocarbon feedstocks, because the spectral intensity of the plume dropped sharply as the distance from the nitrogen plasma jet increased. Also, data from the three separate spectrometers used to observe different spectral regions have been scaled so that strong peaks in the violet can be presented on the same graph as weaker peaks at longer wavelengths. This plume was observed for powers above 1500 W and exhibited a weak orange/brown color as shown in Figure 7.28c, assumed due to the production of NO₂. Excited nitric oxide and oxygen atoms produced through the Zeldovich reaction



then combine to form NO_2 according to



The reaction occurs for afterglows in cold environments, produced by means of an electrical discharge through air at reduced pressure (Gaydon, 1974). Transitions of NO_2 to the ground state cause visible absorption bands and the brown color of the gas observed during the experiment. In addition, Gaydon notes that in afterglows there are some faint NO_2 emission bands superposed on the continuum, which are shown in Figure 7.26.

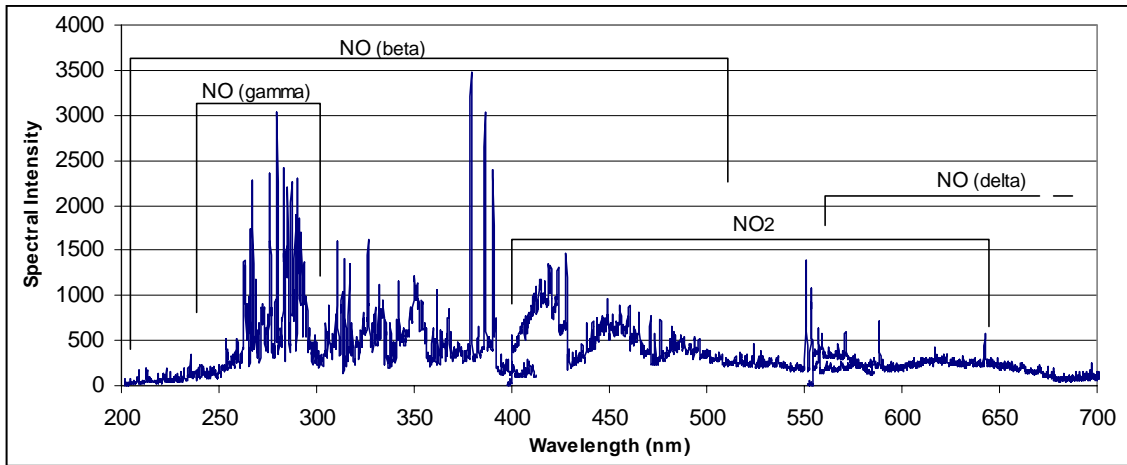


Figure 7.25: Spectrogram of Nitrogen Plume

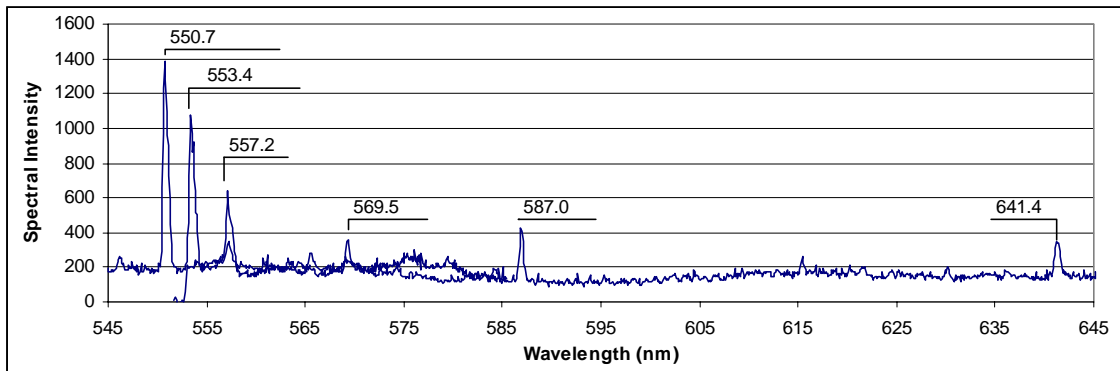


Figure 7.26: Spectral Peaks of NO_2 in the Yellow-Orange Region

In addition to the observation of the NO_2 plume originating from the plasma jet, the plasma jet itself was observed to change color depending on the torch input power.

Powers below 1000 W produced a plasma jet exhibiting a purple color, while at higher powers this color changed to a blue-green, illustrated in Figure 7.27. The flow in this figure is from the lower left to upper right. The purple color of the plasma jet is associated with the Second Positive System of nitrogen, which spans the purple to green region, but is most intense in the purple. At higher powers, the nitrogen afterglow dominates, resulting in the blue-green color observed in Figure 7.27b. The brown colored tip indicates the production of NO_2 as discussed earlier. At higher powers, the concentration of nitrogen atoms increases, increasing the rate of reaction with oxygen molecules from the freestream, and hence the production of NO_2 according to Equation 7.5.

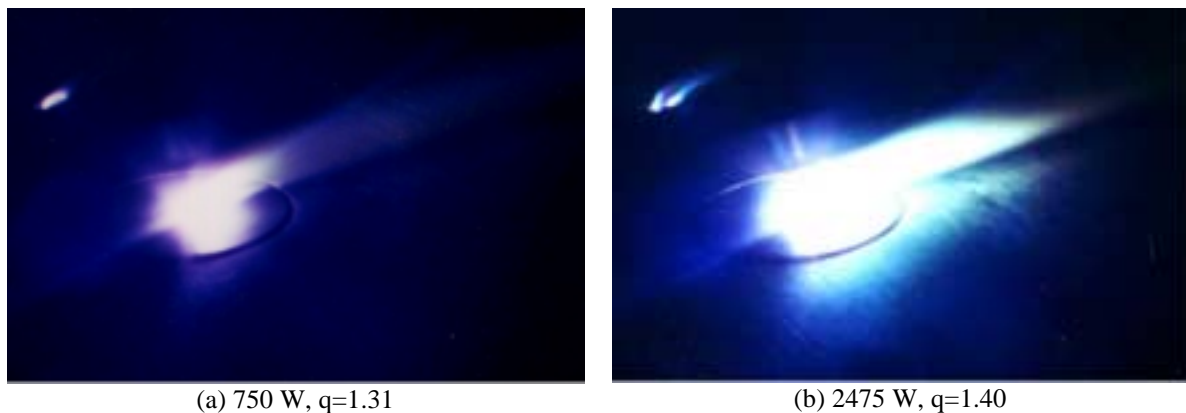


Figure 7.27: Color Variations in the Nitrogen Plasma Jet

In addition to the jet color variation, the plume color also changed with increasing power. As shown in Figure 7.28, the plume changes from a purple color at 660 W, to a purple-blue at 930 W, and the characteristic orange/brown at 1500 W. Here, flow is from left to right and reflections can be seen on the back tunnel wall and on the tunnel floor. The length and intensity of the plume both increase with increasing power. Color variation within the plume indicates a composition change. The purple color produced at lower powers is associated with the intense peaks of the NO_β System, which radiate strongly from 275 to 390 nm. The presence of these peaks is especially strong when oxygen is introduced to active nitrogen, as is the case here. At higher powers, the plume exhibits an orange/brown coloration associated with the production of NO_2 . This

suggests an increase in the concentration of monatomic oxygen and nitric oxide by means of the reaction in Equation 7.4.

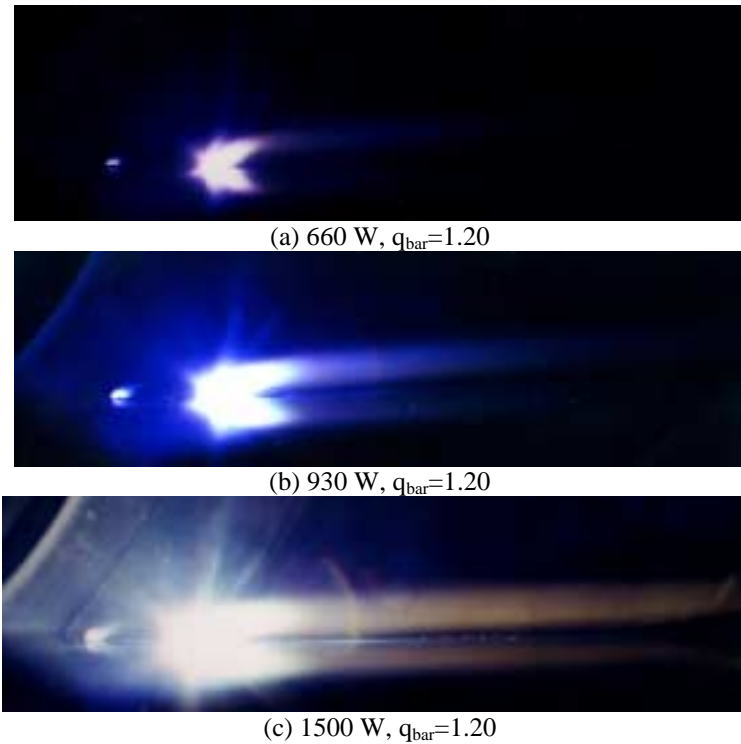


Figure 7.28: Nitrogen Plume Color Variations with Increasing Power

Between 1000 and 1500 W, the plume exhibited a layered appearance. As shown in Figure 7.29, a purple layer associated with NO appears above an orange/brown layer, which is produced by NO₂. The layered plume structure is a function of both the reactions governing the production of NO and NO₂, as well as the structure of the plasma jet. The jet itself also exhibits a layered structure with an identifiable sublayer along the tunnel floor. From the photograph it is clear that the two plumes originate from these two regions. It appears that the NO₂ plume is trapped in the shear layer, which provides a subsonic region for the reactions governing the production of NO₂ to take place. At higher powers the energy content and concentration of participating species is great enough that the subsonic region is no longer required to sustain the NO₂ reactions.



Figure 7.29: A Nitrogen Plume with a Layered Structure at 1250 W

To study the composition of the layered plume, the spectrometer was used to measure the emission of excited NO and NO₂ downstream of the plasma jet. Figure 7.30 shows the distribution of the spectral intensity of a line from the NO_β system at 380.1 nm. The spectral maximum of the NO_β profile occurs 3.5 mm above the tunnel floor, close to where the boundary between the two plumes is observed in Figure 7.29. Below this maximum, the orange region visually dominates, but the intensities of the NO₂ lines in the orange were much weaker than the NO lines in the purple. This suggests that the NO₂ in this region is not strongly excited, and may only reflect the light from the torch and the excited NO region above it.

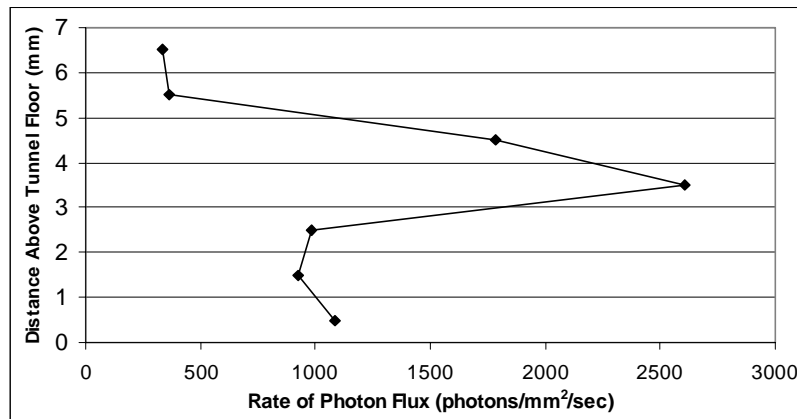


Figure 7.30: NO Distribution of Nitrogen Plume 1.25 cm Downstream of Torch Exit (750 W, $q_{\text{bar}}=1.24$)

Total temperature measurements were used to determine how the thermal energy of the plasma jet was being mixed into the freestream. Centerline temperature measurements for nitrogen are shown in Figure 7.31. As with other feedstock gases, increases in power produce a linear increase in the measured total temperature ratio, and does not appear to significantly affect the penetration height. Comparison to methane

and ethylene shows that, for the same power, nitrogen plumes exhibit much lower total temperature ratios. As an example, nitrogen at 1500 W produces a maximum total temperature ratio of 1.16, whereas for methane the ratio is 1.26. As discussed earlier, this is a direct result of the specific heat of the feedstock gas, where the specific heat of nitrogen is about half that of methane at 1000 K. However, it should be noted that the ignition potential of a plasma torch has very little to do with the thermal energy content of the plasma and much more to do with the concentration of combustion enhancing radicals. For the present setup, the profiles are more indicative of the penetration height of the thermal energy, and are also a qualitative measure of the efficiency at a particular power.

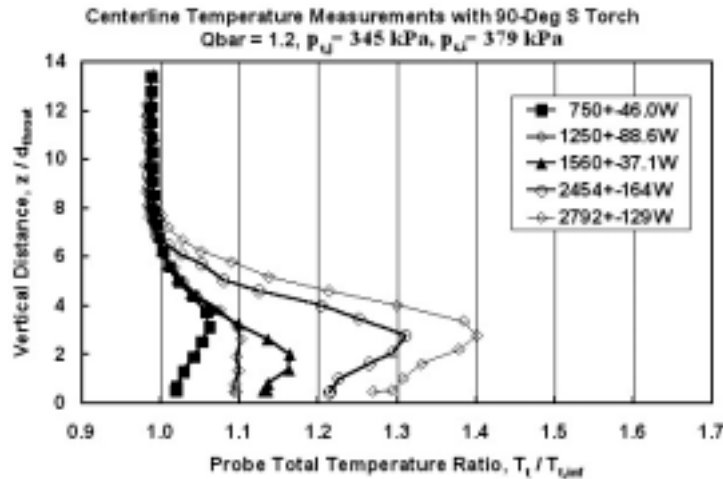


Figure 7.31: Centerline Temperature Profiles for Nitrogen

Two 2D total temperature profiles are shown in Figure 7.32 for powers of 750 and 1500 W. As expected, the maximum observed total temperature ratio increases from 1.07 to 1.16 for the higher power. Comparison of the two profiles shows radically different plume shapes. The 750-W profile exhibits the characteristic mushroom-like appearance, where the plume core has shifted slightly to the left due to the induced swirl. The 1500-W profile exhibits two hot spots, one where the plume core is expected, and another along the tunnel floor to the left of the main plume. The arc attachment point produced this second hot spot, which for these runs was located on the left side of the constrictor exit. A dull orange plume, like those shown in Figure 7.28c and 7.29, was observed to emanate from this point, and corresponds well with the temperature measurements made downstream. Although not a common occurrence, this is a demonstration that the arc

attachment point plays a critical role in the performance of the design, and if manipulated properly, could produce effects that are not otherwise normally observed with traditional designs.

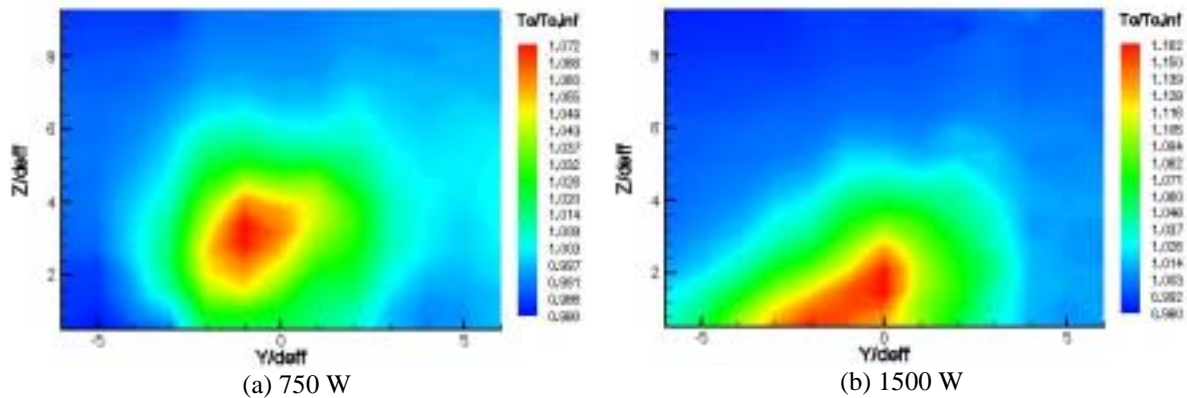


Figure 7.32: Two-Dimensional Temp Profiles for Nitrogen

7.3: Conclusions

Experimental tests in quiescent and supersonic environments were conducted to study the performance of the 90°, 2.54-mm throat length design, as well as collect fundamental data associated with the performance of plasma torches in supersonic flow. Quiescent experiments focused heavily on spectrographic investigation of the plasma jet, along with high-speed filtered photography to support the spectrographic work. Supersonic experiments conducted in an unheated Mach 2.4 crossflow used spectrography and total temperature measurements to study the performance of the design for varying flowrates, input powers, and feedstock type. To support the spectrographic and temperature measurements, high-speed filtered photography, video observations, shadowgraph and surface oil-flow techniques were used. An abundance of data pertaining to operation of plasma torches in a crossflow was collected, particularly on how the performance of such a design changes with feedstock flowrate, feedstock type, and torch input power.

The main result from the spectrographic analysis in the quiescent environment was that increasing the feedstock flowrate and decreasing the torch power both served to decrease the spectral intensity of the excited species within the plasma jet. The effect of reducing power was attributed to a subsequent decrease in the energy density, while the

increase in mass flowrate caused an increase in the thermal mass of the system. In addition, neither power nor flowrate changes were observed to have a significant effect on the propagation distance of excited hydrogen. High-speed filtered photography demonstrated that CN and OH molecules exhibit a luminous “hoop” structure rather than a solid profile characteristic of a hydrocarbon fragment. This hoop structure was formed by the interaction of the hot plasma with air along the edges of the plasma jet, and was observed to rotate with the arc. Further investigation showed that the plasma jet exhibited a shape similar to an arrowhead, rather than that of a perfect cone. The edges of this arrowhead are free to interact with the surrounding air, producing OH and CN through plasma-air reactions, while the flat surfaces are surrounded by methane, preventing such reactions.

High-speed photography in the supersonic environment showed evidence of electrode particle ejection while operating on methane. These particles were observed to propagate much further into the crossflow than the plasma jet, leading to the idea that these particles could act as micro-flameholders and be supplied by a consumable cathode design. Shadowgraph and surface oil-flow techniques were used to study the effect of torch input power and feedstock flowrate on the shape and strength of the bow shocks and separation zones. Measurement of the bow shock angle showed that increases in the torch power produced subsequent increases in the bow shock angle. This was attributed to a volume effect, produced by both an increase in the total temperature of the feedstock gas and the reduction of the molecular weight through dissociation. Increases in the mass flowrate were observed to have a negligible effect on the bow shock, demonstrating that for the conditions tested, the thermal energy of the torch has a much larger influence on the angle of the bow shock than mass addition. Furthermore, oil flow visualization showed that increases in both the mass flowrate and power of the torch pushed the bow shock further upstream, increasing the size of the separation zone upstream of the torch orifice.

Tests with ethylene and nitrogen demonstrated similar spectrographic trends to methane, in that the intensity of the plasma jet exhibited a linear dependence on the torch input power. Furthermore, for a given power, ethylene produced nearly identical hydrogen intensities as methane. Through total temperature probing, it was shown that

the specific heat of the feedstock gas has a strong influence on the amount of energy the feedstock gas extracts from the arc. Ethylene, with the highest specific heat of the three gases tested, also produced the highest total temperature ratios. Plumes of excited species were also observed for each of the three gases. Spectrographic analysis of the combustion plumes from methane showed the presence of combustion products H_2O and CO_2 , as well as various intermediates such as OH and HCO . The nitrogen plume was associated with the formation of NO_2 by means of excited nitric oxide reacting with diatomic oxygen.